Thermal energy storage behaviour of 3D ceramic/molten salt structures under real concentrated solar radiation

Irene Díaz-Herrezuelo, Pilar Miranzo, Audrey Soum-Glaude, Christophe Escape, Quentin Falcoz, Manuel Belmonte

Journal of the European Ceramic Society 45 (2025) 116975

Contents lists available at ScienceDirect

Journal of the European Ceramic Society

journal homepage: www.elsevier.com/locate/jeurceramsoc

Thermal energy storage behaviour of 3D ceramic/molten salt structures under real concentrated solar radiation

Irene Díaz-Herrezuelo [a], Pilar Miranzo [a], Audrey Soum-Glaude [b], Christophe Escape [b], Quentin Falcoz [b,c,**], Manuel Belmonte [a,*]

[a] Institute of Ceramics and Glass (ICV, CSIC), Kelsen 5, Madrid 28049, Spain
[b] Laboratory of Processes, Materials and Solar Energy (PROMES-CNRS, UPR 8521), 7 rue du Four Solaire, Font-Romeu Odeillo 66120, France
[c] University of Perpignan Via Domitia (UPVD), 52 avenue Paul Alduy, Cedex 9, Perpignan 66860, France

ARTICLE INFO

Keywords:
Thermal energy storage
Concentrated solar power
Additive manufacturing
Phase change materials
Ceramics

ABSTRACT

Molten salts, phase change materials commonly employed in thermal energy storage (TES) systems, are widely known to enhance the efficient use and storage of solar energy in concentrated solar power (CSP) plants. Here, three-dimensional TES (3DTES) have been manufactured from highly porous (up to ~90 %) 3D printed patterned vermiculite (V) and alumina (Al_2O_3) supports, which have been infiltrated with molten sodium nitrate salt (nn) and solar salt (ss). These 3DTES have been validated under real concentrated solar radiation in a parabolic solar furnace. Among the different 3DTES, those based on V-nn exhibits the best efficiency for the conversion of the incident solar radiation into heat; whereas Al_2O_3-nn transfers the heat more efficiently and allows a faster charging-discharging cyclability due to its higher thermal conductivity. This study confirms the benefits of additive manufacturing to develop a new class of innovative TES for CSP applications.

1. Introduction

The current increasing energy global consumption linked to the use of fossil fuels has prompted the search for alternative environmentally friendly approaches that can stabilize the power grid and reduce greenhouse gas emissions. Renewable energy sources provide a clean and sustainable solution to energy demands. In this context, concentrated solar power (CSP) emerges as a promising and competitive technology to mitigate the elevated cost of electricity [1–3]. CSP can dispatch high amounts of energy by employing the huge solar radiation. Compared to the photovoltaic technology, which can convert the solar radiation directly into electricity, the main advantage of CSP is that it can be coupled with thermal energy storage (TES) systems to produce and store energy in form of heat 24 hours a day, regardless the weather conditions, releasing the thermal energy to produce the electricity on demand [4].

TES systems have several advantages compared to other energy storage technologies, such as lower capital costs and very high operating efficiencies [5]. They stock thermal energy by heating or cooling a reservoir for further use in thermal applications and power generation [6]. Thermal energy can be stored as a change in the internal energy of the reservoir material as latent heat, sensible heat, thermochemical and a combination of all of them [7]. Latent heat storage (LHS) uses the enthalpy of a phase change material (PCM) to store large amounts of energy [8]. In particular, solid-liquid phase transformations offer better efficiencies and are suitable for medium-high temperature applications, such as those attained in CSP, at low operational costs. Although the most widespread TES technologies use only sensible heat storage (SHS), LHS has attracted great attention in recent years because it provides higher energy storage densities than SHS [1]. Other advantages of LHS are the wide range of PCM available, its high thermal efficiency, and nearly isothermal operation at the phase transition temperature [9]. However, their overall thermal performance is limited by their usually low thermal conductivity, the liquid leakage in the molten state and corrosion issues [10,11]. One of the strategies to minimize these problems is the PCM encapsulation or infiltration into porous supports, in particular, ceramics such as porous clay powders or mesoporous silica foams [12], leading to the development of form-stable composite PCM

* Corresponding author.
** Corresponding author at: Laboratory of Processes, Materials and Solar Energy (PROMES-CNRS, UPR 8521), 7 rue du Four Solaire, Font-Romeu Odeillo 66120, France.
E-mail addresses: quentin.falcoz@promes.cnrs.fr (Q. Falcoz), mbelmonte@icv.csic.es (M. Belmonte).

https://doi.org/10.1016/j.jeurceramsoc.2024.116975
Received 13 September 2024; Received in revised form 4 October 2024; Accepted 5 October 2024
Available online 9 October 2024

(FSPCM) [8,13,14]. Recently, some of the present authors have reported the additive manufacturing of robust and highly porous patterned 3D ceramic supports infiltrated with sodium nitrate ($NaNO_3$) salts, known as 3DTES, as a promising alternative to solve the lacks of PCM also improving the energy storage performance [15,16].

The aim of the present work is to move a step forward and validate, for the first time, the 3DTES approach under relevant and real concentrated solar radiation using a very specific solar furnace at PROMES-CNRS. In this way, two types of large ceramic supports with different thermal conductivity, vermiculite and alumina (Al_2O_3), have been additive manufactured by robocasting, a direct ink writing technology, to be infiltrated with two distinct molten salts commonly employed in CSP applications; in particular, $NaNO_3$, a low-cost salt with high thermal capabilities, low supercooling and a melting temperature of ~307 ºC, and solar salt, a binary mixture of $NaNO_3$ and KNO_3 (60:40 in weight) with a melting point of ~222 ºC that allows working in a wider temperature range due to its high decomposition temperature (565 ºC) [17]. Solar salt is also commonly used as sensible heat storage material in conventional CSP plants. The energy stored, solar absorptance, thermal emittance, heliothermal efficiency, thermal conductivity and heat transfer coefficient of the developed 3DTES have been investigated.

2. Materials and methods

2.1. Manufacturing of 3DTES

The development of printable expanded vermiculite (V) and boehmite (B) inks, the latter as precursor of the Al_2O_3 scaffolds, was reported elsewhere [16,18]. Briefly, a pseudoplastic V ink containing, in weight, 36.3 % of clay, 9.1 % of activated carbon (AC) employed as a pore former, and 54.6 % of ultrapure water, was formulated; whereas the B ink was produced with 52.0 wt.% of solids and 48.0 wt.% of ultrapure water. Unframed cylindrical structures with a linear array of 9 parallel filaments on the X-Y plane and between 130 (V) and 160 (B) layers orthogonally assembled respect to the adjacent layer on the z-direction were computed designed with a CAD software (RoboCAD 4.2, 3-D Inks LLC). The dimensions of the scaffold design varied as a function of the materials (20.3 mm in diameter and 62.3 mm in height for V supports, and 24 mm in diameter and 76.7 mm in height for B structures) taking into account their different shrinkage during the further thermal treatments. The goal was to produce scaffolds with a final diameter of 20 mm and 50 mm in height in both cases.

The inks were extruded through a nozzle tip with an inner diameter of 610 μm, at room temperature in air onto flat alumina substrates, and using a three-axis robocasting system (A3200, 3-D Inks LLC) at a constant speed of 10 $mm{\cdot}s^{-1}$. The as-printed scaffolds were dried in air for 24 h and, then, heat treated under distinct temperature conditions. V scaffolds were heated at 800 ºC for 1 h to remove the water, burn out the activated carbon and partially sinter the structures; while B supports were sintered in air at 1300 ºC for 2 h to fully transform the boehmite into α-Al_2O_3 crystalline phase. The geometrical density (ρ_{geo}) was calculated from the weight and dimensions of the ceramic scaffold; whereas the total porosity (π_{total}) of the 3D support was obtained using the equation $\pi_{total} = 100\ x\ (1 - \rho_{geo}/\rho_{th})$, being ρ_{th} the theoretical density of each support (2.60 $g{\cdot}cm^{-3}$ for V and 3.98 $g{\cdot}cm^{-3}$ for α-Al_2O_3). Besides, the porosity associated to the open channels of the patterned design, or 3D porosity (π_{3D}), was calculated using the geometrical parameters; whereas the porosity of the ceramic struts, labelled as rod porosity (π_{rod}), was determined from the expression: $\pi_{rod} = 100\ x\ (\pi_{total} - \pi_{3D})/(100 - \pi_{3D})$.

The PCM wettability on the supports was investigated by placing a compacted cube (3 mm in diameter and 3 mm in height) of each PCM on a bulk vermiculite or alumina plate (15 ×7×2 mm^3) and using a heating microscope (HR18 model, Axel Hesse Instruments). The tests were carried out in air, up to 250 ºC (solar salt) and 320 ºC ($NaNO_3$), and employing a heating rate of 5 $ºC{\cdot}min^{-1}$.

The infiltration step with $NaNO_3$ and solar salt was carried out in an electric furnace in air conditions at ~ 50 ºC above the melting point of each PCM, i.e., at 350 ºC and 270 ºC, respectively. The 3D support was completely submerged for 30 min into an alumina crucible containing the fully molten salt. Afterwards, the scaffold was removed and left to cool down at room temperature. Three different 3DTES were produced, in particular, V-nn, V-ss and Al_2O_3-nn ("nn" and "ss" correspond to $NaNO_3$ and solar salt, respectively). The encapsulation capacity of the 3D ceramic supports (η_e) was assessed for each PCM from the expression: η_e (%) = 100 x ($W_{3DTES} - W_{3D}$)/W_{3DTES}, where W_{3DTES} and W_{3D} refer to the weights of the 3DTES and ceramic supports, respectively. The melting temperature (T_{melt}), enthalpy of fusion (ΔH) and specific heat when the PCM is in the solid ($\overline{C}_{p\ sol}$) and liquid states ($\overline{C}_{p\ liq}$) were obtained by differential scanning calorimetry (DSC, Discovery DSC, TA Instruments). The DSC tests were conducted from room temperature up to 350 ºC for scaffolds infiltrated with $NaNO_3$, and up to 270 ºC for those infiltrated with solar salt, using nitrogen as purge gas. Heating/cooling rates of 5 $ºC{\cdot}min^{-1}$ (for T_{melt} and ΔH) and 10 $ºC{\cdot}min^{-1}$ (for C_p) were employed. Optical stereomicroscopy (Nikon SMZ1000) was used to observe in detail the microstructure of the infiltrated scaffolds.

2.2. Parabolic solar furnace experiments

The medium size solar furnace used (MSSF at PROMES-CNRS) consists of a parabolic mirror of 1.5 m in diameter. The MSSF has a maximum total power of 850 W at the focal point, considering a direct normal irradiation (DNI) of ~1000 $W{\cdot}m^{-2}$, which is defined as the amount of solar radiation received per unit area by a surface that is always normal to the Sun's rays [19]. In the present work, the experiments were carried out with a DNI of 968 ± 26 $W{\cdot}m^{-2}$. The solar beams were directly reflected from the Sun to the MSSF through a solar mirror or heliostat that can be aligned in the NS (north-south) and EW (east-west) axes in order to track the Sun thanks to a servo-electric motor system (Fig. 1a).

To study the heat front propagation, each 3DTES specimen was gently ground to achieve a final height of 44 mm and, then, placed at the focal point of the parabola into a mobile platform. The schematic configuration of the MSSF installation is shown in Fig. 1b. Five thermocouples (from T1 to T5, RS Pro 363–0250, Z2-K-1M-MP) were laterally introduced in holes drilled (1 cm in depth and 1 mm in diameter) through the 3DTES outer wall (Fig. 1c), starting at 2 mm (T1) from the top of the sample to avoid the thermocouple to be directly under the solar radiation. The rest of thermocouples (T2-T4) were equispaced about 10.5 mm towards the bottom of the specimen (Fig. 1c). The last thermocouple (T5) did not require a hole as it was located at the bottom of the scaffold. Therefore, five cylindrical regions (from R1 to R5, Fig. 1c) can be established for the further energy analysis. The temperature of each region was supposed to be radially uniform at the temperature of its corresponding thermocouple. All thermocouples were connected to a temperature sensor (Graphtec, midi LOGGER GL 220). The temperature (T) was represented versus the time (t) for each thermocouple, obtaining T(t) curves in which the charging-steady state-discharging processes can be observed. These curves were also employed to assess the heat transfer coefficient. The MSSF was equipped with a trap or door and an external/manual controlled shutter that can be tuned from 0 to 100 %, allowing regulating the solar input power.

3DTES specimens were introduced into a stainless steel (Grade 310) cylinder and an Inconel 625 cover with Pyromark paint (solar absorber) was used to homogenize the heat on the 3DTES top receiving surface (Fig. 1c). Since the solar irradiation forms a cone at the focal point with a spot diameter of about 10 mm, the top surface of the 3DTES was shifted ~12 mm above the focal point to ensure the whole 3D specimen surface (20 mm in diameter) received the solar irradiation. The shutter was first opened by 2 % at a time, which means an input solar power of 3.8 ± 0.1 W taking into account the power interpolation as a function of the

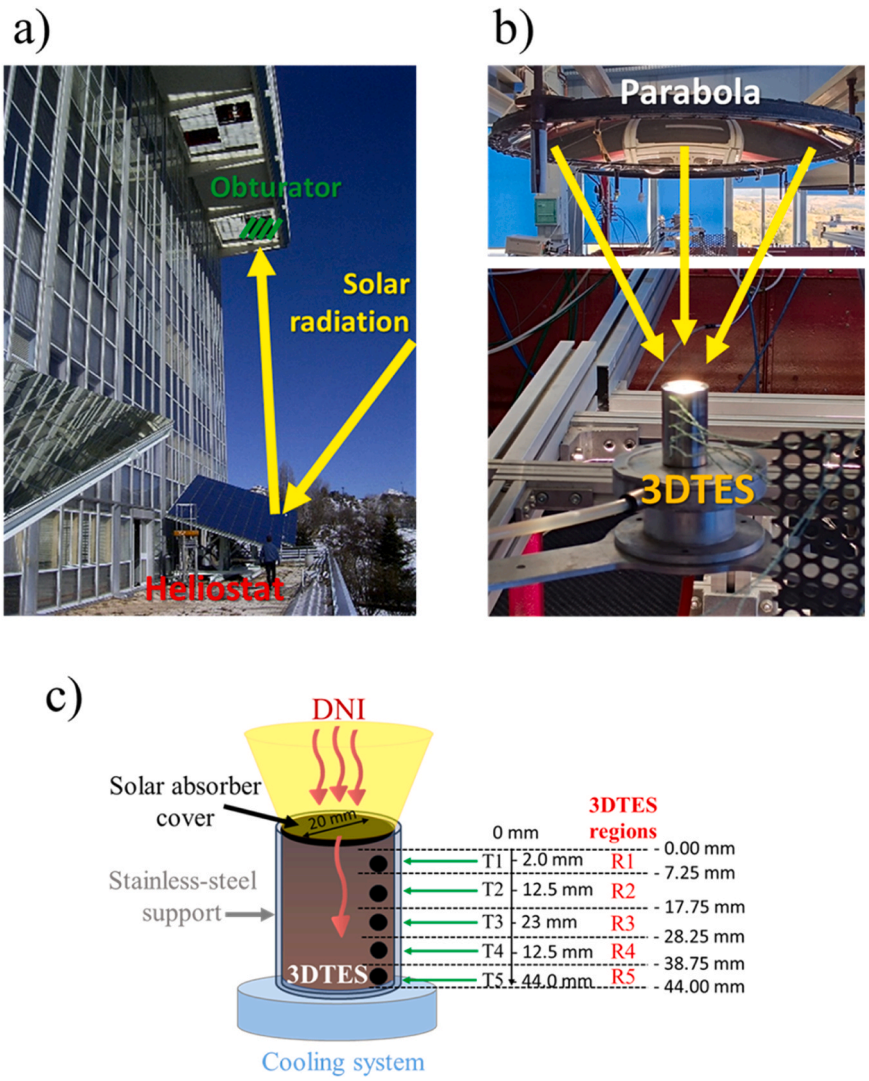

Fig. 1. a) Building with the solar installation, including the heliostat and the obturator. b) Solar parabola reflecting the solar beams (yellow arrows) directly to the 3DTES specimen. c) Schematic configuration of the 3DTES for running the solar experiments, where the thermocouples (T1-T5) location along the specimen in the different established regions (R1-R5) of the specimen are shown.

shutter's opening (Figure S1) and the average DNI on each solar parabola experiment. Then, the obturator was gradually opened by 1 % every 5 min until the maximum temperature for thermocouple T1, associated to the corresponding melting temperature of the infiltrated PCM, was reached. As result, the maximum apertures for 3DTES-nn and 3DTES-ss were 12 % (solar power = 34.0 ± 0.5 W) and 14 % (solar power = 41.6 ± 1.7 W), respectively. The steady state was maintained at least 30 min to guarantee the thermal stabilization of all thermocouples. A cooling system at the bottom of the metallic support avoided the overheating of the experimental set-up during the charging and steady-state steps; whereas free cooling down took place during the discharging process.

2.3. Optical and thermal properties of 3DTES

The solar absorptance (α_s) of 3DTES was derived from the spectral reflectance measurements at room temperature, which were carried out in two wavelength ranges: 0.250–2.5 μm (Perkin Elmer Lambda 950) and 1.25–25 μm (SOC-100 HDR reflectometer, Surface Optics Corporation, coupled with a Nicolet FTIR 6700 spectrophotometer), using cylindrical samples of 20 mm in diameter and 12 mm in height. In this way, for opaque materials with no transmission, α_s was calculated from:

$$\alpha_s = \frac{\int [1 - R(\lambda)] \cdot G(\lambda) \cdot d\lambda}{\int G(\lambda) \cdot d\lambda} \quad (1)$$

where R(λ) is the spectral reflectance and G(λ) the standard solar irradiance spectrum (ASTM G173–03 AM1.5 Direct + circumsolar Reference Spectrum [20]). Additionally, the thermal emittance (ε(T)) was also calculated for the different 3DTES using the following equation:

$$\varepsilon(T) = \frac{\int [1 - R(\lambda)] \cdot M^0_\lambda(\lambda, T) \cdot d\lambda}{\int M^0_\lambda(\lambda, T) \cdot d\lambda} \quad (2)$$

where $M^0_\lambda(\lambda, T)$ is the blackbody spectrum at the average maximum temperature measured during solar experiments, i.e., 360 °C for 3DTES-nn and 430 °C for 3DTES-ss, as derived from Plank's law [21].

The thermal diffusivity (α_T) was measured by the Laser Flash method (LFA, Netzsch, 457 Instrument) up to 270 °C for samples infiltrated with $NaNO_3$, and up to 180 °C for those containing the solar salt. The thermal conductivity (k_T) was then calculated from α_T according to the following expression:

$$k_T(T) = \alpha_T(T) \cdot C_p(T) \cdot \rho_{geo}(T) \quad (3)$$

Top and bottom faces of the samples were ground to achieve 10.3

$\times 10.3\ mm^2$ on the x-y plane and a thickness of 2.7 mm and, afterwards, the specimens were coated with graphite to improve the energy absorption/emission at the surface. The measurements were carried out under Argon atmosphere (Argon flux of 1000 $cm^3 \cdot min^{-1}$) with a heating rate of 5 $C \cdot min^{-1}$. The reported data correspond to three consecutive measurements with an interval of 5 min between each shoot.

3. Results and discussion

3.1. 3DTES characterization

Table 1 collects some of the main microstructural parameters of the different heat treated 3D supports, including the filament diameter (d_{rod}), width of the open channels ($w_{channel}$), ρ_{geo} and the main porosity parameters. 3D V supports were much lighter (0.25 $g \cdot cm^{-1}$) than the corresponding 3D Al_2O_3 ones (0.47 $g \cdot cm^{-1}$), and both of them exhibited quite similar values of π_{total} (~ 90 %) and π_{3D} (~76 %). The 3D vermiculite skeleton was formed by filaments of 0.48 mm in diameter spanned 1.29 mm; whereas, in the case of the Al_2O_3 supports, the channel width was slightly higher (1.35 mm) as a consequence of a larger shrinkage of this ceramic skeleton (22 % and 55 % for V and B as-printed supports, respectively) during the sintering process that led to slightly thinner (0.43 mm in diameter) and denser filaments. In fact, π_{rod} was lower for the 3D Al_2O_3 structure (52.9 %) than for the vermiculite one (60.4 %).

The encapsulation capacity and some thermal parameters of the distinct 3DTES are summarized in Table 2. As it can be seen, η_e for V-nn was higher (80.7 wt.%, 82.8 vol.%) than for Al_2O_3-nn (64.7 wt.%, 76.3 vol.%). Taking into account that the wettability of the $NaNO_3$ salt on both ceramic supports is quite similar (Figure S2), that encapsulation difference can be explained by a distinct η_e into the filaments due to differences in π_{rod} of the vermiculite and Al_2O_3 structures. In this way, considering that the patterned structures for both supports were mostly infiltrated by the molten PCM, i.e., η_e associated to the channels would be alike π_{3D}, the encapsulation into the ceramic skeletons would be 7.3 vol% for V-nn and 0.5 vol% for Al_2O_3-nn. In addition, it seems that $NaNO_3$ and solar salt present a good and comparable wettability (Figure S2) to the vermiculite support as η_e was alike for both V 3DTES (~80 wt.%). Despite the molten PCM filled the open channels of the supports, the 3D structures appeared infiltrated just about 54 % of the total height in the solid state after the solidification step (Fig. 2) due to the liquid-solid volume shrinkage of the PCM (18 % for $NaNO_3$ [22] and 12 % for the solar salt [23]). This means that only R1-R3 regions contained PCM encapsulated into the open channels of the 3DTES and, thus, R4 and R5 were discarded in the further analysis of the thermal energy storage.

Data of enthalpy of fusion are directly related to both the PCM encapsulation and the ΔH value of the pure salt ($\Delta H_{NaNO3} = 178.4\ J \cdot g^{-1}$, $\Delta H_{solar\ salt} = 110.7\ J \cdot g^{-1}$). In this way, ΔH for V-nn was about 12 % higher (147.4 $J \cdot g^{-1}$) than for Al_2O_3-nn (131.8 $J \cdot g^{-1}$); whereas the enthalpy for V-ss reached a value of 93.9 $J \cdot g^{-1}$, a 36 % lower latent heat storage than for V-nn. Then, the latent thermal energy storage efficiency (E_s) for each 3DTES was estimated using the melting (m) and solidifying (s) enthalpies of the pure salts and the 3DTES according to the following equation: $E_s = 100\ x\ [\Delta H_{3DTES,\ m)} + (\Delta H_{3DTES,\ s)}] / [\Delta H_{PCM,\ m)} + (\Delta H_{PCM,\ s)}]$. As result, E_s for V-nn, V-ss and Al_2O_3-nn reached values of 86.7, 83.6 and 76.6 %, respectively.

Table 1
Geometrical density (ρ_{geo}), total porosity (π_{total}), 3D porosity (π_{3D}), rod porosity (π_{rod}) and diameter (d_{rod}), and channel width ($w_{channel}$) of the heat treated 3D vermiculite (V) and Al_2O_3 supports.

3D support	ρ_{geo} ($g \cdot cm^{-3}$)	π_{total} (%)	π_{3D} (%)	π_{rod} (%)	d_{rod} (mm)	$w_{channel}$ (mm)
V	0.25 ± 0.1	90.3 ± 0.3	75.5 ± 0.7	60.4 ± 0.3	0.48 ± 0.01	1.29 ± 0.07
Al_2O_3	0.47 ± 0.2	88.6 ± 0.6	75.8 ± 0.5	52.9 ± 1.5	0.43 ± 0.01	1.35 ± 0.03

3.2. 3DTES performance under real concentrated solar radiation

A representative example of the temperature increment with time of the thermocouples placed along the height of V-nn, V-ss and Al_2O_3-nn during the MSSF tests is shown in Fig. 3 (see plots of all experiments in Figure S3).

Considering the decomposition temperatures for the $NaNO_3$ (380 ºC) and the solar salt (565 ºC) [17], the solar irradiation received on the 3DTES specimens was controlled to reach during the tests a maximum temperature (T_{max}) in the thermocouple T1 around 360 ºC for V-nn (361 ± 18 ºC) and Al_2O_3-nn (355 ± 17 ºC); while a value of T_{max} of 429 ± 21 ºC was attained for V-ss. The charging, steady-state, and discharging processes can be clearly seen in the T(t) curves of Fig. 3. In this way, the heating rate, i.e., the slope, during charging decreased with the distance from the heat source (i.e., from T1 to T5), and the same behaviour was observed for the cooling rate during the discharging process. A constant temperature response was recorded for all thermocouples and specimens during the steady-state region (Fig. 3). As result, T1 and T2 measurements during the steady-state for V-ss were above the solar salt melting temperature and then R1 and R2 were melted; but for both 3D supports infiltrated with $NaNO_3$ only T1 was above the corresponding melting temperature and, then, just the first region (R1) of the 3DTES was melted.

In order to calculate the total stored energy after the charging phase (E_{stored}) of the different 3DTES, the contributions of the sensible heat storage, in the temperature range below (solid state) and above (liquid state) the melting point, and of the latent heat storage, during the solid-liquid phase transition, must be considered. The percentage of molten PCM in each region for the distinct 3DTES (Table S1), considering only T1, T2 and T3, was calculated knowing the height of the sample (or distance to the top surface) where the melting point is located and the PCM encapsulation in R1, R2 and R3. The position of the melting point can be established with the corresponding temperature profiles in the steady-state region (Fig. 4), taking into account the temperature difference between each experimental value and the ambient temperature (θ), which was about 13–14 ºC due to the cooling system. The PCM loss after the solar experiments was 1.1 % for V-nn and Al_2O_3-nn, and 5.7 % for V-ss. The reason for the higher loss in the case of V-ss could be explained by its larger percentage of molten PCM in the 3DTES (71.3 %, Table S1), as compared to that in V-nn (27.9 %) and Al_2O_3-nn (25.0 %), which was due to its higher volume (R1 and R2 regions) of the former 3DTES at a temperature above the melting point. In view of all these issues, E_{stored} for the regions containing molten salts was calculated using the following equation:

$$E_{stored} = M_{SHS,s} \cdot \overline{C}_{psol} \cdot (T_{melt} - T_{amb}) + M_{LHS} \cdot \Delta H + M_{SHS,l} \cdot \overline{C}_{pliq} \cdot (T_{max} - T_{melt}) \quad (4)$$

where M is the 3DTES mass (Table S1) contributing to the SHS in the solid ($M_{SHS,s}$) and liquid ($M_{SHS,l}$) states, and also to the LHS (M_{LHS}); T_{amb} is the ambient temperature, and $\overline{C}_{p\ sol}$ and $\overline{C}_{p\ liq}$ are the average specific heat from T_{melt} to T_{max} that was fitted to 360 ºC for V-nn and Al_2O_3-nn and 430 ºC for V-ss (data collected in Table 2). In the case of regions having unmolten PCM, only the first term is considered and T_{melt} should be replaced by T_{max}. Besides, the energy storage density per unit mass (Q) can be assessed as $Q = E_{stored}/M$, where M is the total 3DTES mass included in the R1, R2 and R3 regions.

Comparing 3DTES infiltrated with the same PCM (Table 3), i.e., $NaNO_3$, a slightly better (~10 %) energy storage density response -both E_{stored} and Q- was obtained for the vermiculite support than for the Al_2O_3 one, a consequence of its larger SHS and LHS contributions (Table S1). Despite V-ss presented lower enthalpy and specific heat

Table 2
Encapsulation capacity (η_e) of 3DTES. The thermal parameters considering R1-R3 regions in the specimens are also included, in particular, the melting temperature (T_{melt}), enthalpy of fusion (ΔH), latent thermal energy storage efficiency (E_s) and specific heat when the PCM is in the solid ($\overline{C}_{p\ sol}$) and liquid ($\overline{C}_{p\ liq}$) phases.

3DTES	η_e (wt.%)	η_e (vol.%)	T_{melt} (°C)	ΔH ($J{\cdot}g^{-1}$)	E_s (%)	$\overline{C}_{p\ sol}$ ($J{\cdot}g^{-1}{\cdot}K^{-1}$)	$\overline{C}_{p\ liq}$ ($J{\cdot}g^{-1}{\cdot}K^{-1}$)
V-nn	80.7 ± 0.5	82.8 ± 0.5	306.4	147.4	86.7	1.45	1.56
V-ss	80.0 ± 1.4	82.6 ± 1.4	222.4	93.9	83.6	1.42	1.53
Al_2O_3-nn	64.7 ± 0.9	76.3 ± 0.9	306.8	131.8	76.6	1.44	1.61

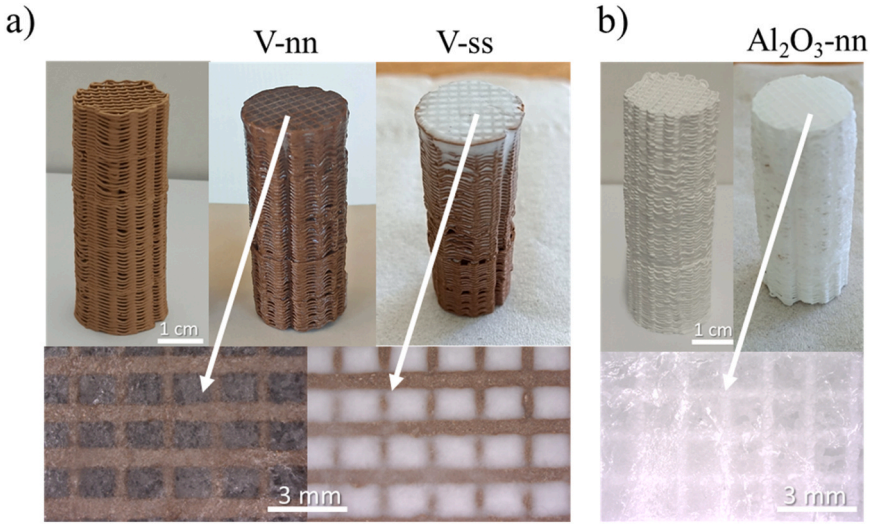

Fig. 2. Optical views of the 3D structures before and after the infiltration process with the molten salts for: a) V-nn and V-ss, and b) Al_2O_3-nn. Detailed views of the top surfaces of the 3DTES are also shown in the images at the bottom of the panel.

values than V-nn, E_{stored} was comparable because T_{max} reached a higher value (up to 430 °C).

The solar absorptance, obtained by integrating the reflectivity spectrum (Fig. 5), for V-nn, V-ss and Al_2O_3-nn was ~69 %, ~42 % and ~23 % (Table 4), respectively, which evidenced a clear effect of the 3D support (higher α_s for the vermiculite support using the same PCM) and, to a lesser extent, also of the PCM, as $NaNO_3$ led to a larger α_s than the solar salt for the same 3D support. The thermal emittances were quite similar for all 3DTES (Table 4), slightly lower for V-ss. Based on these results, it can be concluded that V-nn presented the best optical performance under relevant solar radiation. From α_s and ε (T), the theoretical heliothermal efficiency ($\eta_{heliothermal}$) was calculated to quantify the efficiency for the conversion of the incident solar radiation into heat as [21]:

$$\eta_{heliothermal} = \alpha_s - \frac{\varepsilon(T)\cdot\sigma(T^4 - T_0^4)}{C\cdot I\cdot\eta_{opt}} \quad (5)$$

where σ is the Stefan-Boltzman constant, T is 633 K for V-nn and Al_2O_3-nn and 703 K for V-ss, T_0 is 273 K, C relates to the solar concentration ratio (100), I is referred to the incident solar flux density (900 $W{\cdot}m^{-2}$), and η_{opt} is the concentrator solar efficiency (0.8). As seen in Table 4, V-nn exhibited a good solar-to-thermal conversion response ($\eta_{heliothermal}$ ~67 %), three times larger than that obtained for the 3DTES using the same salt but distinct support (Al_2O_3-nn, $\eta_{heliothermal}$ ~20 %). Besides, the $NaNO_3$ salt almost doubled this energy conversion parameter as compared with the solar salt, taking into account that T for the latter was even higher.

The thermal conductivity as a function of temperature was assessed using the thermal diffusivity (Figure S4), the density and the specific heat of 3DTES (Table S2). The densities varied depending on the state of the infiltrated PCM. In this way, the values in the solid state (experimentally measured) were 2.05 $g{\cdot}cm^{-3}$ (V-nn), 1.79 $g{\cdot}cm^{-3}$ (V-ss) and 2.07 $g{\cdot}cm^{-3}$ (Al_2O_3-nn); while in the liquid state they were calculated employing the molten salt content into the 3DTES, the density of the ceramic support, and the density of the molten PCM at each temperature using data from literature for $NaNO_3$ [22] and solar salt [23]. In addition, the density of the ceramic supports was considered constant within the temperature range analysed. Regarding the thermal diffusivity, α_T value at each region of the 3DTES was interpolated from the experimental curve (Figure S4) when the temperature was below T_{melt}; whereas α_T data above T_{melt} were estimated employing the α_T dependence with the temperature reported in the literature for "nn" [22] and "ss" [24]. Fig. 6 plots k_T for V-nn, V-ss and Al_2O_3-nn at the different temperatures recorded in each thermocouple (numerical data collected in Table S3). As expected, the larger conductivity of Al_2O_3 as compared to vermiculite led to a higher k_T value of the corresponding 3DTES. In this way, Al_2O_3-nn exhibited 40–50 % higher k_T than V-nn in the whole range of temperatures tested, varying from a maximum value at 56 °C (T5) of 1.31 $W{\cdot}m^{-1}{\cdot}K^{-1}$ to 0.36 $W{\cdot}m^{-1}{\cdot}K^{-1}$ at 354 °C (T1). Comparing both salts on 3D vermiculite supports, and taking into account that the PCM encapsulation is similar for V-nn and V-ss, the infiltration with $NaNO_3$ enhanced the conductivity of the 3DTES due to the higher k_T of the pure $NaNO_3$ (1.39 $W{\cdot}m^{-1}{\cdot}K^{-1}$ at 25 °C and 0.87 $W{\cdot}m^{-1}{\cdot}K^{-1}$ at 180 °C [16]) than that of the molten salt (1.25 $W{\cdot}m^{-1}{\cdot}K^{-1}$ at 25 °C and 0.71 $W{\cdot}m^{-1}{\cdot}K^{-1}$ at 180 °C [25]). The increment observed at 450 °C for V-ss is related to higher thermal diffusivity estimated for this salt (Figure S4).

An important parameter during the steady-state process is the heat transfer coefficient (h), which is related to the ability that the 3DTES surface has to transfer heat to its surroundings, and can be calculated from the equation [26]:

$$h = m^2 \cdot k_T \cdot r / 2 \quad (6)$$

where r is the radius of the 3DTES, k_T is the thermal conductivity

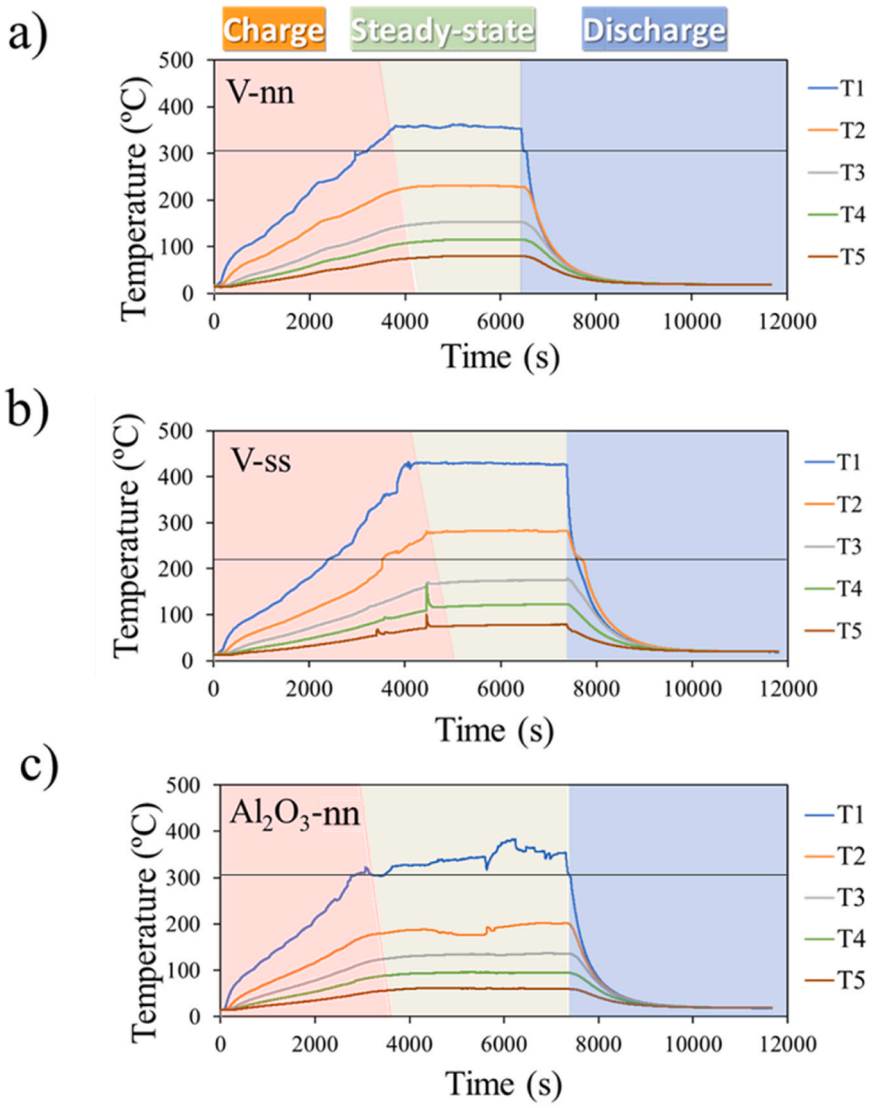

Fig. 3. Representative temperature-time curves for each thermocouple (T1-T5) in: a) V-nn, b) V-ss and c) Al_2O_3-nn showing the charge, steady-state and discharge regions. A horizontal line corresponding to the melting temperature of the corresponding PCM is also included in the plots.

averaged from the thermal conductivity values for each region in the specimens (Table 4), and m is referred to the temperature decay with the distance from the irradiated surface of the 3DTES (Fig. 4), and corresponds to the exponent of the exponential fitting (Table 4). In addition,

$$\theta(x) = \theta_i \cdot e^{-m \cdot x} \quad (7)$$

θ_i being the maximum temperature difference between the top and the bottom part of the 3DTES. A deeper explanation of those equations can be found in the Figure S5 of the Supporting Information.

Data shown in Table 4 indicate that Al_2O_3-nn would transfer the heat more efficiently than V-nn, with a h value almost twice than that for V-nn (11.7 vs 6.2 $W \cdot m^{-2} \cdot K^{-1}$). This result can be explained by its higher k_T that would lead to a faster charging-discharging cyclability. The response as a function of the type of salt using the same support is less remarkable, with about 20 % of increment in the h parameter when the PCM was $NaNO_3$, coinciding with smaller differences in k_T.

θ/θ_i versus the time (t) in the discharging region for the distinct 3DTES was plotted in Fig. 7 to evaluate the release of the thermal energy, where θ and θ_i corresponds to T_{exp}-T_{amb} and T_{max}-T_{amb}, respectively. Only regions containing molten PCM were considered, i.e., R1 for 3DTES-nn and R1 plus R2 for V-ss. 3DTES-nn curves (Fig. 7a) exhibited an initial decrease of the temperature with the time until reaching an inflection point where the slope drastically reduced, which is linked to the liquid-solid phase transition of $NaNO_3$ (the melting temperature is represented by a straight line). The crystallization of the salt occurred in a short period of time without a significant variation in the temperature. This behaviour, enlarged in Fig. 7b, kept around 60 s for V-nn; while it lasted only half as long (30 s) for Al_2O_3-nn, which can be attributed to its higher thermal conductivity. In the case of V-ss, the change in the slope was observed in R2 (Fig. 7c), as the phase transition of the solar salt took place in this region, and it lasted ~ 300 s (Fig. 7d).

All curves were fitted to an expression based on the Newton's Law of Cooling in the form of $e^{-t/\tau}$; where τ, namely time constant, is the time in which the temperature decays to 37 % of its initial value and gives an idea of how fast the 3DTES is discharged. The lower the τ parameter the faster the energy is released, which is convenient for CSP applications. As it can be seen in Table 5, the thermal time constant in R1 for Al_2O_3-nn ($\tau_1 = 424$ s) was slightly lower than for V-nn ($\tau_1 = 440$ s), which would indicate that the former 3DTES would induce a faster release of the energy due to its higher thermal conductivity and heat transfer coefficient (Table 4). For V-ss, a similar τ_1 than for V-nn was attained in the first region (446 s, fully melted region). However, the phase change occurred in R2, with a τ_2 of 507 s, leading to the slowest release of the energy (lower k_T and h parameters).

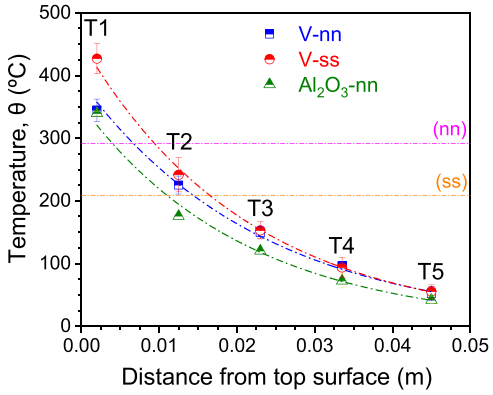

Fig. 4. Temperature profile within the 3DTES in the steady-state process for V-nn (square), V-ss (circle) and Al_2O_3-nn (triangle). The temperature difference (θ) between each experimental value and the ambient temperature (13–14 ºC) is plotted versus the distance of the different thermocouples (T1 to T5) to the top irradiated surface of the specimen. The melting temperatures of $NaNO_3$ (nn) and solar salt (ss) minus the T_{amb} were highlighted by a straight line. Data were fitted (dashed lines) to an exponential decay using an equation in the form of $\theta(x) = \theta_i \cdot e^{-m \cdot x}$.

Table 3
Energy storage density per mass-unit (Q) and energy stored density (E_{stored}) for the different 3DTES.

3DTES	Q ($J \cdot g^{-1}$)	E_{stored} (kJ)
V-nn	443 ± 18	5.6 ± 0.3
V-ss	474 ± 28	5.7 ± 0.4
Al_2O_3-nn	408 ± 8	5.1 ± 0.1

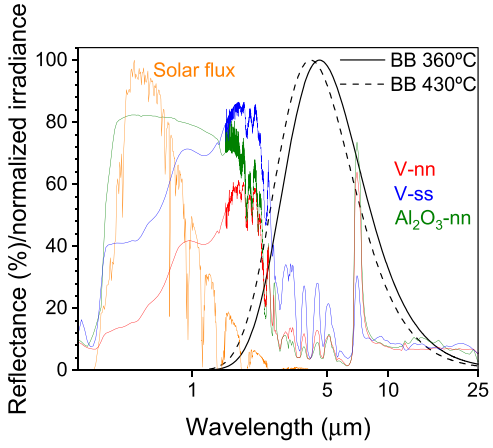

Fig. 5. Spectral reflectance ($R(\lambda)$) for the different 3DTES (V-nn, V-ss and Al_2O_3-nn). The blackbody spectrum (BB) at 360 ºC and 430 ºC and the solar flux have also been included.

4. Conclusions

3DTES have been manufactured in a two-step process consisting of direct ink writing of light and highly porous 3D vermiculite and Al_2O_3 supports and subsequent infiltration with molten nitrate-based salts. 3D vermiculite supports allows reaching PCM encapsulation capacities up to ~80 wt.%, superior than for 3D Al_2O_3 supports (65 wt.%) and independently of the selected molten salt, due to a larger infiltration degree of the salt into the vermiculite struts. As a result, and due to its larger sensible and latent heat storage contributions, V-nn has about 10 % better energy storage density response in terms of E_{stored} and Q than Al_2O_3-nn. All 3DTES do not show significant liquid leakage of the encapsulated molten salt after the parabolic solar furnace tests.

The combination of vermiculite supports and $NaNO_3$ salt leads to 3DTES with the best optical performance under relevant solar radiation (α_s = 69.3 %) and solar-to-thermal conversion response ($\eta_{heliothermal}$ ~67 %) from the set of developed 3DTES. Conversely, Al_2O_3-nn presents 40–50 % higher thermal conductivity than V-nn in the 25–270 ºC temperature interval due to the contribution of the ceramic support, leading to about two times more efficient heat transfer (h = 11.7 $W \cdot m^{-2} \cdot K^{-1}$) and, hence, faster charging-discharging cyclability. Consequently, the release of the energy is the fastest for Al_2O_3-nn, decreasing for V-nn and V-ss. The results open a promising approach through additive manufacturing strategies for the development of novel TES based on high temperature molten salts for CSP applications.

CRediT authorship contribution statement

Manuel Belmonte: Writing – original draft, Supervision, Funding acquisition, Formal analysis, Data curation, Conceptualization. **Pilar Miranzo:** Writing – original draft, Formal analysis, Data curation. **Irene Diaz-Herrezuelo:** Writing – original draft, Methodology, Investigation, Formal analysis, Data curation. **Christophe Escape:** Investigation, Data curation. **Audrey Soum-Glaude:** Investigation, Data curation. **Quentin Falcoz:** Writing – original draft, Investigation, Formal analysis, Data curation, Conceptualization.

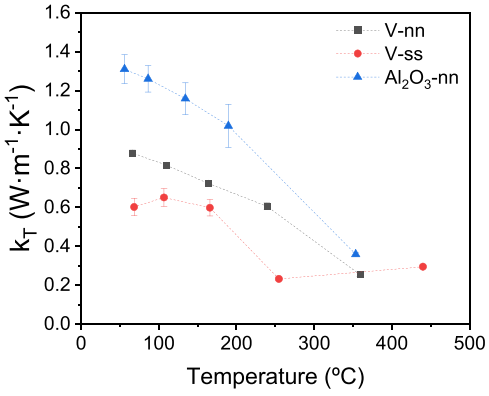

Fig. 6. Thermal conductivity (k_T) variation with the temperature in each thermocouple for V-nn (black square), V-ss (red circle) and Al_2O_3-nn (blue triangle).

Table 4
Optical and thermal parameters of 3DTES. Solar absorptance (α_s), thermal emittance (ε(T)), heliothermal efficiency ($\eta_{heliothermal}$), heat transfer coefficient (h), averaged thermal conductivity (k_T) for the whole 3DTES specimens, temperature difference between the top and the bottom part of the 3DTES (θ_i), exponential fitting (m) to the Eq. (7), and maximum temperature reached at the top of the 3DTES ($T_{(x=0)}$) were also included.

3DTES	α_s (%)	ε(T) (%)	$\eta_{heliothermal}$ (%)	h ($W \cdot m^{-2} \cdot K^{-1}$)	k_T ($W \cdot m^{-1} \cdot K^{-1}$)	θ_i (ºC)	m (m^{-1})	$T_{(x=0)}$ (ºC)
V-nn	69.3	88.5	66.9	6.2 ± 2.3	0.66 ± 0.25	390.0 ± 31.8	43.4 ± 5.0	404.0 ± 31.8
V-ss	41.8	83.8	38.4	5.2 ± 2.2	0.47 ± 0.20	453.6 ± 17.0	47.0 ± 4.0	466.6 ± 17.0
Al_2O_3-nn	22.7	88.0	20.2	11.7 ± 4.8	1.04 ± 0.39	352.7 ± 24.3	47.6 ± 5.0	366.7 ± 24.3

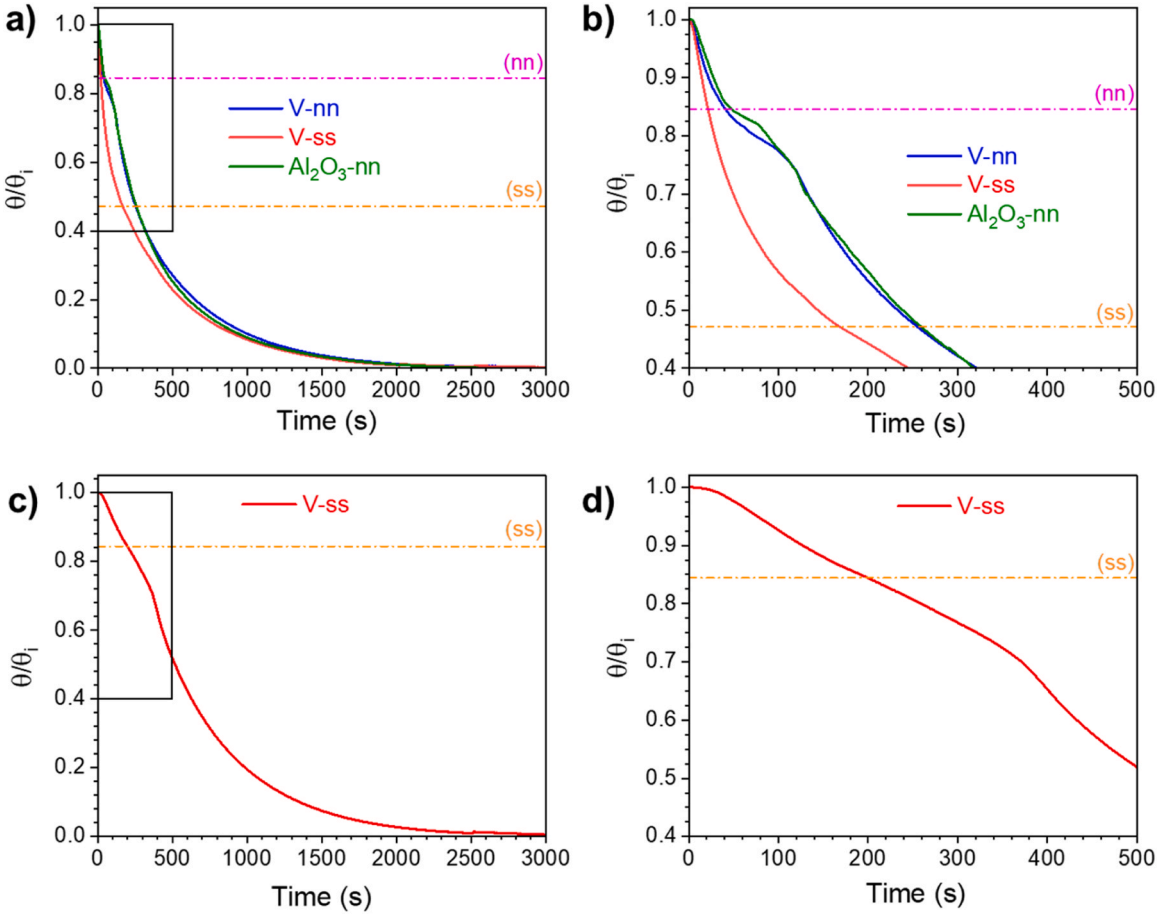

Fig. 7. Averaged discharging curves for the different 3DTES in R1 (a,b) and R2 (c,d) by plotting θ/θ_i versus the time (t). The plateau due to the solidification process (framed with a rectangle) in R1 and R2 is enlarged in (b) and (d), respectively. The melting temperatures of $NaNO_3$ (nn) and solar salt (ss) were highlighted by a straight line.

Table 5
Thermal time constant (τ) in R1 and R2 for the different 3DTES.

3DTES	τ_1 (s)	τ_2 (s)
V-nn	440 ± 58	—
V-ss	446 ± 107	507 ± 76
Al_2O_3-nn	424 ± 6	—

Declaration of Competing Interest

The authors declare that they have no known competing financial interests or personal relationships that could have appeared to influence the work reported in this paper.

Acknowledgments

This work was supported by MCIN/AEI/ 10.13039/501100011033 and by "ERDF A way of making Europe" through Grant PID2021–125427OB-I00; and by the French "Investments for the future" program managed by the National Agency for Research under contract ANR-10-EQPX-49-SOCRATE. I. D.-H. is grateful to the JECS Trust for funding the visit to PROMES-CNRS laboratory (Contract No. 2023357).

Appendix A. Supporting information

Supplementary data associated with this article can be found in the online version at doi:10.1016/j.jeurceramsoc.2024.116975.

References

[1] S. Pascual, P. Lisbona, L.M. Romeo, Thermal energy storage in concentrating solar power plants: a review of European and North American R&D projects, Energies 15 (2022) 8570, https://doi.org/10.3390/en15228570.
[2] K.M. Kennedy, T.H. Ruggles, K. Rinaldi, J.A. Dowling, L. Duan, K. Caldeira, N. S. Lewis, The role of concentrated solar power with thermal energy storage in least-cost highly reliable electricity systems fully powered by variable renewable energy, Adv. Appl. Energy 6 (2022) 100091, https://doi.org/10.1016/j.adapen.2022.100091.
[3] M.I. Khan, F. Asfand, S.G. Al-Ghamdi, Progress in research and technological advancements of commercial concentrated solar thermal power plants, Sol. Energy 249 (2023) 183–226, https://doi.org/10.1016/j.solener.2022.10.041.
[4] X. Py, N. Sadiki, R. Olives, V. Goetz, Q. Falcoz, Thermal energy storage for CSP (concentrating solar power), EPJ Web Conf 148 (2017) 00014, https://doi.org/10.1051/epjconf/201714800014.
[5] S. Kuravi, J. Trahan, D.Y. Goswami, M.M. Rahman, E.K. Stefanakos, Thermal energy storage technologies and systems for concentrating solar power plants, Prog. Energ. Combust. 39 (2013) 285–319, https://doi.org/10.1016/j.pecs.2013.02.0.
[6] I. Sarbu, C. Sebarchievici, A comprehensive review of thermal energy storage, Sustainability 10 (2018) 191, https://doi.org/10.3390/su10010191.
[7] A. Kumar, S.K. Shukla, A review on thermal energy storage unit for solar thermal power plant application, Energy Procedia 74 (2015) 462–469, https://doi.org/10.1016/j.egypro.2015.07.728.
[8] X. Huang, X. Chen, A. Li, D. Atinafu, H. Gao, W. Dong, G. Wang, Shape-stabilized phase change materials based on porous supports for thermal energy storage applications, Chem. Eng. J. 356 (2019) 641–661, https://doi.org/10.1016/j.cej.2018.09.013.
[9] D.S. Jayathunga, H.P. Karunathilake, M. Narayana, S. Witharana, Phase change material (PCM) candidates for latent heat thermal energy storage (LHTES) in concentrated solar power (CSP) based thermal applications – a review, Renew. Sustain. Energy Rev. 189 (2024) 113904, https://doi.org/10.1016/j.rser.2023.113904.
[10] V. Goel, A. Dwivedi, R. Kumar, R. Kumar, A.K. Pandey, K. Chopra, V.V. Tyagi, PCM-assisted energy storage systems for solar-thermal applications: Review of the

associated problems and their mitigation strategies, J. Energy Storage 69 (2023) 107912, https://doi.org/10.1016/j.est.2023.107912.
[11] C. Xu, H. Zhang, G. Fang, Review on thermal conductivity improvement of phase change materials with enhanced additives for thermal energy storage, J. Energy Storage 51 (2022) 104568, https://doi.org/10.1016/j.est.2022.104568.
[12] J.T. Gao, Z.Y. Xu, R.Z. Wang, Experimental study on a double-stage absorption of solar thermal storage system with enhanced energy storage density, Appl. Energy 262 (2020) 114476, https://doi.org/10.1016/j.apenergy.2019.114476.
[13] S. Höhlein, A. König-Haagen, D. Brüggemann, Macro-encapsulation of inorganic phase-change materials (PCM) in metal capsules, Materials 11 (2018) 1752, https://doi.org/10.3390/ma11091752.
[14] W. Liu, Y. Bie, T. Xu, A. Cichon, G. Królczyk, Z. Li, Heat transfer enhancement of latent heat thermal energy storage in solar heating system: a state-of-the-art review, J. Energy Storage 46 (2022) 103727, https://doi.org/10.1016/j.est.2021.103727.
[15] I. Diaz-Herrezuelo, L. Moreno-Sanabria, P. Miranzo, M.I. Osendi, M. Belmonte, Novel 3D thermal energy storage materials based on highly porous patterned printed clay supports infiltrated with molten nitrate salts, Addit. Manuf. 59 (2022) 103108, https://doi.org/10.1016/j.addma.2022.103108.
[16] I. Díaz-Herrezuelo, P. Miranzo, M.I. Osendi, M. Belmonte, High thermal energy storage efficiency of molten salts fully encapsulated into additive manufactures cellular vermiculite scaffolds, J. Energy Storage 85 (2024) 111108, https://doi.org/10.1016/j.est.2024.111108.
[17] Y.T. Wu, Y. Li, N. Ren, C.F. Ma, Improving the thermal properties of $NaNO_3$-KNO_3 for concentrating solar power by adding additives, Sol. Energy Mater. Sol. Cells 160 (2017) 263–268, https://doi.org/10.1016/j.solmat.2016.10.013.
[18] C. Ramírez, M. Belmonte, P. Miranzo, M.I. Osendi, Reinforced 3D composite structures of γ-Al_2O_3 with carbon nanotubes and reduced GO ribbons printed from boehmite gels, Materials 14 (2021) 2111, https://doi.org/10.3390/ma14092111.
[19] A. Thumann, D.P. Mehta. Handbook of Energy Engineering, 7th edition, River Publishers, Gistrup, Denmark, 2020, https://doi.org/10.1201/9781003151715.
[20] ⟨https://www.nrel.gov/grid/solar-resource/spectra.html⟩.
[21] A. Soum-Glaude, A. Le Gal, M. Bichotte, C. Escape, L. Dubost, Optical characterization of $TiAlN_x$/$TiAlN_y$/Al_2O_3 tandem solar selective absorber coatings, Sol. Energy Mater. Sol. Cells 170 (2017) 254–262, https://doi.org/10.1016/j.solmat.2017.06.007.
[22] T. Bauer, D. Laing, R. Tamme, Characterization of sodium nitrate as phase change material, Int. J. Thermophys. 33 (2012) 91–104, https://doi.org/10.1007/s10765-011-1113-9.
[23] T. Bauer, N. Pfleger, N. Breidenbach, M. Eck, D. Laing, S. Kaesche, Material aspects of solar salt for sensible heat storage, Appl. Energy 111 (2013) 1114–1119, https://doi.org/10.1016/j.apenergy.2013.04.072.
[24] P. Zhang, J. Cheng, Y. Jin, X. An, Evaluation of thermal physical properties of molten nitrite salts with low melting temperature, Sol. Energy Mater. Sol. Cells 176 (2018) 36–41, https://doi.org/10.1016/j.solmat.2017.11.011.
[25] I. Díaz-Herrezuelo, Q. Falcoz, A. Soum-Glaude, M. Belmonte, Solar salt encapsulated into 3D printed activated carbon/alumina supports for thermal energy storage applications, Open Ceram 19 (2024) 100648, https://doi.org/10.1016/j.oceram.2024.100648.
[26] F.P. Incropera, D.P. Dewitt, T.L. Bergman, A.S. Lavine. Fundamentals of Heat and Mass Transfer, 6th ed., John Wiley & Sons, New York, 2007, pp. 137–161.